Research Square

Preprints are preliminary reports that have not undergone peer review.
They should not be considered conclusive, used to inform clinical practice,
or referenced by the media as validated information.

Estimating cotton leaf area index under shallow subsurface drip irrigation using TabPFN and UAV-based multisource remote sensing

fujun meng
Tarim University
Yu Zhou
Tarim University
Xingpeng Wang
Tarim University
Yujin Liu
Tarim University
Aijun Sun
Tarim University
Yasengjiang Kahaer
Tarim University
Shengru Yue
nmgndysr@163.com
Tarim University

Research Article

Keywords: TabPFN, shallow subsurface drip irrigation, leaf area index, UAV-based multisource remote sensing, SHAP

Posted Date: November 3rd, 2026

DOI: https://doi.org/10.21203/rs.3.rs-10873743/v1

License: This work is licensed under a Creative Commons Attribution 4.0 International License.
Read Full License

Additional Declarations: No competing interests reported.

Estimating cotton leaf area index under shallow subsurface drip irrigation using TabPFN and UAV-based multisource remote sensing

Fujun Meng[a,b1], Yu Zhou[a,b1], Xingpeng Wang[a,b,c*], Yujin Liu[a], Aijun Sun[a,b,c], Yasengjiang Kahaer[a,b], Shengru Yue[a,b*].

[a] College of Water Hydraulic and Architectural Engineering, Tarim University, Alar, Xinjiang 843300, China.

[b] Key Laboratory of Comprehensive Utilization of Saline-Alkali Land, Xinjiang Production and Construction Corps, Alar, Xinjiang 843300, China.

[c] Tarim Institute of Eco-Environment Protection and Restoration, Alar, Xinjiang 843300, China.

*Corresponding authors: Xingpeng Wang (13999068354@163.com) and Shengru Yue (nmgndysr@163.com)

Abstract: Leaf area index (LAI) is a key indicator of cotton canopy development and crop water status, yet its accurate estimation under shallow subsurface drip irrigation in arid regions remains challenging because spatial variability in soil moisture and salinity increases canopy heterogeneity. This study integrated UAV-based hyperspectral and RGB imagery with Tabular Prior-data Fitted Network (TabPFN) to estimate cotton LAI under small-sample conditions. Spectral vegetation indices, colour indices, and texture features were extracted, and stable predictors were selected using recursive feature elimination with cross-validation. Stage-specific models for the squaring, flowering, boll-development, and boll-opening stages were developed from hyperspectral, RGB, and fused feature sets. TabPFN was compared with XGBoost, random forest, and support vector regression, and SHapley Additive exPlanations (SHAP) quantified feature contributions. Across the 12 growth-stage–feature-set combinations, TabPFN performed best overall (mean $R^2 = 0.781 \pm 0.190$). Multisource fusion was strongly stage dependent: relative to the best-performing single-source feature set, fusion increased R^2 by 1.2%, 7.1%, and 12.2% at squaring, flowering, and boll development, respectively, but performed slightly worse than hyperspectral features at boll opening. SHAP revealed clear

stage-specific shifts in feature importance: texture dominated at squaring, photochemical indices were most influential at flowering and boll opening, and pigment-related and structural features jointly contributed at boll development. Field-scale LAI maps generated with the optimal models revealed pronounced spatial differences among irrigation treatments. Combining TabPFN with UAV-based multisource remote sensing can provide accurate and interpretable cotton LAI estimates under small-sample conditions, thereby supporting crop monitoring and precision irrigation in arid regions.

Keywords: TabPFN; shallow subsurface drip irrigation; leaf area index; UAV-based multisource remote sensing; SHAP

1. Introduction

Cotton (*Gossypium hirsutum L.*) is one of the world's most important natural fibre crops (USDA Foreign Agricultural Service, 2024). China is among the leading cotton-producing countries and accounts for approximately 20–24% of global cotton production (OECD/FAO, 2025). Within China, Xinjiang accounts for nearly 90% of the national cotton-planted area, with southern Xinjiang contributing more than half of the total and serving as a major region for high-quality cotton production (Gale et al., 2022; Kang et al., 2023). Although plastic-mulched drip irrigation has increased cotton yields in recent decades, residual plastic film levels in some fields have reportedly exceeded 24%, degrading soil structure and threatening long-term agricultural sustainability (Roy et al., 2011; Duan et al., 2021). Shallow subsurface drip irrigation (SSDI) has therefore received increasing attention as an alternative. However, under the arid and saline–alkaline conditions of southern Xinjiang, SSDI faces substantial challenges, including accelerated water loss, surface salt accumulation, and reduced water-use efficiency (Mou et al., 2011; Wan et al., 2024). Effective management of soil moisture and salinity therefore requires rapid, dynamic monitoring of crop canopy development.

Leaf area index (LAI) is closely related to canopy structure, photosynthetic capacity, and crop water status and is therefore an important indicator for SSDI management (Fang et al., 2019; Yang et al., 2025). Conventional ground-based measurements are labour intensive and

time consuming, making them unsuitable for large-scale, dynamic monitoring (Yang et al., 2025). UAV-based multisource remote sensing enables flexible acquisition of high-resolution phenotypic data and has become a widely used tool for crop monitoring (Yang et al., 2025; Yang et al., 2017). Integrating spectral, colour, and texture information can improve LAI estimation by capturing complementary canopy-reflectance and spatial-structural characteristics (Li et al., 2019; Liu et al., 2021; Sun et al., 2023). In cotton, spectral transformation and the fusion of multiple vegetation indices have improved LAI estimation (Ma et al., 2022; Fan et al., 2024). However, UAV-based multisource fusion for cotton LAI estimation under SSDI remains insufficiently evaluated, and the consistency of fusion benefits across growth stages is unclear. Because separate stage-specific models were developed in this study, only 70 labelled observations were available for model development at each growth stage. In this small-sample, moderately high-dimensional setting, conventional machine-learning algorithms, including random forest (RF), support vector regression (SVR), and extreme gradient boosting (XGBoost), may be sensitive to data partitioning, hyperparameter selection, and overfitting (Vabalas et al., 2019; Hollmann et al., 2025). Variation in growth stage and environmental conditions may further limit model transferability (Yang et al., 2025).

The Tabular Prior-data Fitted Network (TabPFN) offers a promising approach to limited-sample tabular learning. TabPFN is a pretrained foundation model trained on a large collection of synthetic tabular tasks. For a new task, it generates predictions through in-context learning by conditioning on the available labelled observations, without task-specific updates to the pretrained network weights (Hollmann et al., 2025). Its second-generation release, TabPFN-2.5, supports tables with up to 50,000 rows and 2,000 columns (Grinsztajn et al., 2025). To our knowledge, TabPFN has not previously been applied to UAV-based hyperspectral–RGB fusion for estimating cotton LAI under shallow subsurface drip irrigation. Because TabPFN is a complex model, SHapley Additive exPlanations (SHAP) were used to quantify the contributions of individual predictors to stage-specific LAI estimates (Lundberg & Lee, 2017). Separate Spearman correlation analyses were then conducted to explore statistical associations between key remote-sensing features and soil water–salinity variables.

In this study, TabPFN was integrated with UAV-based hyperspectral and RGB remote sensing to estimate cotton LAI under shallow subsurface drip irrigation. The objectives were to (1) develop stage-specific LAI estimation models for the squaring, flowering, boll-development, and boll-opening stages and compare TabPFN with XGBoost, random forest, and support vector regression; (2) apply repeated recursive feature elimination with cross-validation to identify stable feature subsets for each data source and growth stage and evaluate the benefit of multisource fusion relative to single-source features; (3) use SHAP to interpret the contributions of spectral, colour, and texture features and examine their statistical associations with soil water–salinity variables; and (4) generate field-scale LAI maps to characterise spatial variation among irrigation treatments.

2. Materials and methods

2.1 Study area and experimental design

The experiment was conducted during the 2025 cotton-growing season (April–September) at the field experimental station of the Alar Modern Agricultural Academician and Expert Workstation in southern Xinjiang, China (40°32′ N, 81°17′ E; 1100 m a.s.l.) (Fig. 1). The region has a warm-temperate, highly continental arid climate, with a mean annual precipitation of 45 mm, a mean annual temperature of 14.3 °C, and annual evaporation of approximately 2200 mm. The cotton cultivar was Tahe No. 2, an early-maturing cultivar widely grown in southern Xinjiang. Seeds of this cultivar were self-provided by the research group from its own maintained seed stock at Tarim University (Alar, Xinjiang, China); no plant material was purchased from commercial suppliers or collected from the wild. The plant material was formally identified by the research group. All experimental research and field studies on plants, including the use of the plant material, complied with relevant institutional, national, and international guidelines and legislation. A wide–narrow-row planting pattern was used, with wide and narrow row spacings of 66 and 10 cm, respectively. Seven treatments were established, each with three replicates. Six SSDI treatments combined two drip-tape burial depths and three irrigation quotas, whereas conventional mulched surface drip irrigation was included as the control (CK) (Fig. 1c). Drip-tape burial depths were D1 (10 cm) and D2 (20 cm), and irrigation quotas were W1 (225 m^3 ha^{-1}), W2 (300 m^3 ha^{-1}), and W3 (375 m^3 ha^{-1}).

The six SSDI treatments were D1W1, D1W2, D1W3, D2W1, D2W2, and D2W3. The CK treatment received mulched surface drip irrigation at the W3 quota. Irrigation was applied at intervals of 7–10 days.

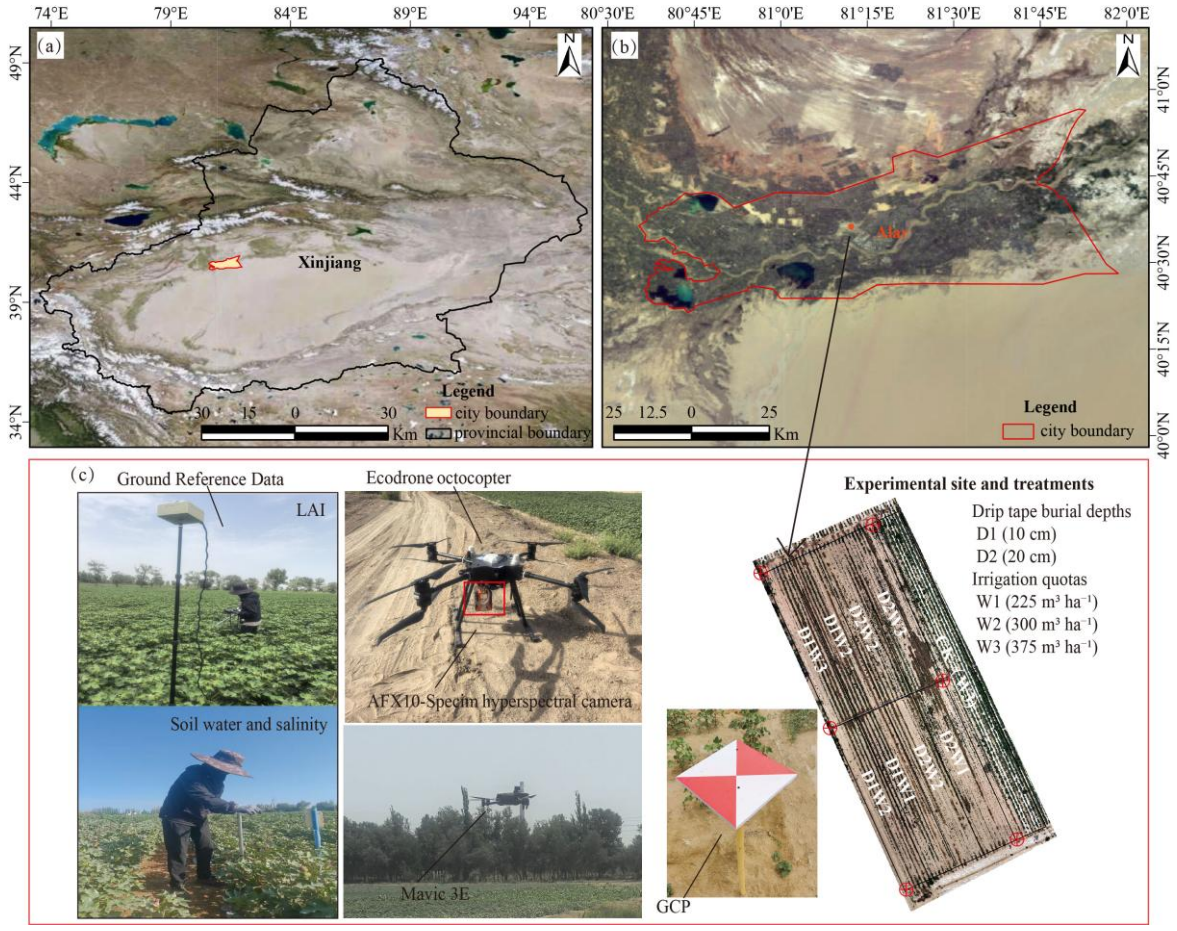


Fig. 1. Study area and experimental design. (a) Location of Xinjiang within China; (b) location of the experimental site in Alar City; and (c) field photographs of the experimental layout and data-collection procedures. Ground measurements included LAI and soil water–salinity sampling. The UAV platforms comprised an Ecodrone octocopter equipped with an AFX10 hyperspectral camera (Specim, Finland) and a DJI Mavic 3E equipped with an RGB camera. Ground control points (GCPs) were deployed for geometric correction and multisource image co-registration.

2.2 UAV data acquisition and preprocessing

Cotton-canopy hyperspectral imagery was acquired using an Ecodrone octocopter UAV (Eco-Tech, China) equipped with an AFX10 hyperspectral imager (Specim, Finland). The instrument records 224 contiguous bands over 400–1000 nm, with a sampling interval of 2.68 nm and a spectral resolution (full width at half maximum, FWHM) of 5.5 nm. Hyperspectral

imagery was acquired at a flight altitude of 70 m, providing a ground sampling distance of approximately 5 cm, with 35% overlap between adjacent flight lines. RGB imagery was acquired using a DJI Mavic 3E equipped with a 20-megapixel 4/3 CMOS camera and a mechanical shutter. RGB flights were conducted at an altitude of 50 m, with forward and side overlaps of 80%.

UAV surveys were conducted at four cotton growth stages: squaring on 14 July (day of year [DOY] 195), flowering on 29 July (DOY 210), boll development on 4 August (DOY 216), and boll opening on 19 August (DOY 231). All flights were conducted between 12:00 and 14:00 local time under clear or partly cloudy conditions, with cloud cover below 10% and wind speeds below 5 m s^{-1}. To support geometric correction and multisource image co-registration, six cross-shaped wooden GCPs (30 cm × 30 cm) were evenly distributed across the experimental field (Fig. 1c). Their coordinates were measured using a CORS-RTK system and expressed in a WGS 84-based Transverse Mercator projected coordinate system with a central meridian of 81° E.

Raw hyperspectral data were processed using CaliGeoPro v2.2 (Eco-Tech, Beijing, China). Radiometric calibration and geometric correction were performed using synchronised navigation data to generate georeferenced radiance images, which were subsequently mosaicked in ENVI 5.3. During each UAV campaign, a calibrated Specim spectral reference panel was placed in the experimental field, and white-reference calibration was used to convert radiance to surface reflectance. The resulting hyperspectral reflectance mosaics were clipped to the experimental area and transformed to the WGS 84-based Transverse Mercator projected coordinate system described above. RGB images were processed in Pix4Dmapper v4.8 using the six GCPs for aerial triangulation, geometric correction, and orthomosaic generation. To ensure spatial consistency during multisource feature extraction, the 5-cm hyperspectral reflectance mosaic was used as the reference grid. The RGB orthomosaic was resampled to 5 cm and aligned with the hyperspectral grid using the same projected extent, pixel size, and pixel origin.

2.3 Ground reference data

2.3.1 LAI measurement

Cotton LAI was measured concurrently with each UAV campaign using a SunScan canopy analyser (Delta-T Devices, Cambridge, UK). Ten fixed sampling locations were established for each treatment, positioned randomly within plots and distributed as evenly as possible among the three replicates to represent within-treatment spatial variability in canopy conditions. The locations were marked during the first survey and repeatedly measured at all four growth stages. At each location, the SunScan probe was positioned beneath the canopy, and three consecutive readings were collected at adjacent positions 10 cm apart. This sequence was repeated three times, yielding nine readings per sampling location. Their mean was used as the reference LAI for that location.

2.3.2 Soil water content and salinity

Soil samples were collected concurrently with LAI measurements. For each treatment, three sampling locations were randomly selected, and samples were collected from three soil layers (0–20, 20–40, and 40–60 cm) using a 5-cm-diameter soil auger. Soil water content (SWC, %) was determined by oven-drying at 105 °C to constant mass. Soil electrical conductivity ($EC_{1:5}$, dS m^{-1}) was measured in a 1:5 soil-to-water extract. Mean values across the three layers were used to represent root-zone soil water–salinity conditions. These data were used to analyse feature responses and support interpretation of the LAI estimation models under contrasting soil water–salinity conditions.

2.4 Feature extraction and selection

All image-derived features were extracted from the co-registered hyperspectral reflectance mosaics and RGB orthomosaics in ENVI 5.3. To match the ground-measured LAI samples, a square region of interest (ROI) of 20 × 20 pixels was centred on each LAI sampling point, corresponding to a ground area of 1.0 m × 1.0 m. The mean pixel value within each ROI was used as the image-derived feature value for the corresponding LAI observation.

2.4.1 Spectral and colour vegetation indices

Twenty-two vegetation indices sensitive to LAI, chlorophyll content, and canopy structure were calculated from the hyperspectral reflectance data, including NDVI, EVI, SAVI, PRI,

ARI, MTCI, NDRE, REP, and VOG. The complete list is provided in Supplementary Table A.1. For indices requiring specific wavelengths, the nearest available hyperspectral bands were used. In addition, 20 colour vegetation indices, including ExG, VARI, GRVI, NGRDI, and CIVE, were extracted from the RGB orthomosaics (Supplementary Table A.2).

2.4.2 Texture features

Grey-level co-occurrence matrix (GLCM) texture features were extracted from the RGB orthomosaics to characterise cotton-canopy spatial structure (Haralick et al., 1973). Before GLCM calculation, RGB images were quantised to 64 grey levels. Texture features were calculated using a 3 × 3 moving window with a pixel offset of 1 in four directions (0°, 45°, 90°, and 135°), and values were averaged across directions. Eight texture metrics were calculated for each RGB band: mean (Mean), variance (VAR), homogeneity (HOM), contrast (CON), dissimilarity (DIS), entropy (ENT), angular second moment (SEC), and correlation (CORR). For each metric, values derived from the R, G, and B bands were averaged, resulting in eight RGB texture features (Supplementary Table A.3).

2.4.3 Feature optimisation and selection

To reduce predictor redundancy and improve feature-selection stability, random-forest-based recursive feature elimination with cross-validation (RFECV) was applied separately to each growth-stage–data-source combination (Guyon et al., 2002). The base estimator comprised 200 trees with a maximum depth of 5. RFECV used shuffled five-fold cross-validation with R^2 as the scoring criterion; one predictor was removed at each iteration, and at least eight predictors were retained. Because feature-selection results can be sensitive to data partitioning and algorithmic randomness, RFECV was repeated 10 times using different random seeds (Nogueira et al., 2018). Predictors retained in at least 60% of the runs were defined as stable features. When fewer than eight predictors met this threshold, the eight predictors with the highest selection frequencies were retained. The resulting stable feature subset was fixed before model evaluation and used consistently for all algorithms within the corresponding growth-stage–data-source combination.

2.5 Model construction and evaluation

2.5.1 Model configuration

Four regression algorithms were evaluated for cotton LAI estimation: TabPFN, extreme gradient boosting (XGBoost), random forest, and support vector regression (SVR) (Chen & Guestrin, 2016; Breiman, 2001; Smola & Schölkopf, 2004). TabPFN was the primary model, whereas the other three algorithms served as benchmarks. TabPFN is a Transformer-based foundation model for tabular data that follows a prior-data-fitted pretraining paradigm and enables rapid prediction on small tabular datasets (Hollmann et al., 2025). We used the TabPFN Regressor implementation in the official Python library with 32 ensemble estimators, a fixed random seed of 42, and GPU acceleration when CUDA was available. TabPFN was applied in its pretrained configuration without task-specific grid search or fine-tuning.

For XGBoost, the search space comprised n_estimators ∈ {100, 200, 300}, max_depth ∈ {3, 5, 7}, and learning_rate ∈ {0.01, 0.1, 0.2}; reg_alpha and reg_lambda were fixed at 0.1 and 1.0, respectively. For random forest, the search space comprised n_estimators ∈ {100, 200, 300} and max_features ∈ {sqrt, log2}; max_depth was fixed at 4 and min_samples_split at 5. For SVR, radial-basis-function and polynomial kernels were compared, with C ∈ {0.1, 1, 10}, gamma ∈ {scale, auto}, and epsilon fixed at 0.1. Feature selection, model training, cross-validation, model interpretation, and batch prediction were implemented in Python 3.13.

2.5.2 Cross-validation and hyperparameter optimisation

For each growth-stage–data-source combination, the stable feature subset identified in Section 2.4.3 was fixed, and all four algorithms used the same predictors and data partitions. Model performance was evaluated using five-fold outer stratified cross-validation. Observations were divided into low-, medium-, and high-LAI groups according to tertiles, and these groups were used to generate shuffled StratifiedKFold splits. The groups were used solely to balance the LAI distribution among folds and were not treated as classification targets.

Within each outer fold, StandardScaler was fitted to the outer training data only and then applied to the corresponding training and test sets. This scaling procedure was used for TabPFN, XGBoost, random forest, and SVR. For the three benchmark models, hyperparameters were selected within the outer training set using shuffled five-fold cross-validation and

GridSearchCV, with R^2 as the optimisation criterion. TabPFN was fitted directly using the prespecified configuration. The outer test fold was used neither to estimate scaling parameters nor to select hyperparameters; it was used only to calculate fold-specific prediction metrics. These procedures were implemented using scikit-learn (Pedregosa et al., 2011).

Stable feature subsets were identified from the complete stage-specific datasets before outer cross-validation. Consequently, the reported results represent internal cross-validation-based model comparisons under fixed stable feature subsets rather than unbiased generalisation estimates obtained through fully nested feature selection or independent external validation (Varma & Simon, 2006). Performance was reported as the mean and standard deviation across the five outer test folds.

2.5.3 Evaluation metrics

Model performance was assessed using three metrics: the coefficient of determination (R^2), root mean square error (RMSE), and mean absolute error (MAE), calculated as follows:

$$R^2 = 1 - \frac{\sum_{i=1}^{n}(y_i - \hat{y}_i)^2}{\sum_{i=1}^{n}(y_i - \bar{y})^2} \quad (1)$$

$$RMSE = \sqrt{\frac{1}{n}\sum_{i=1}^{n}(y_i - \hat{y}_i)^2} \quad (2)$$

$$MAE = \frac{1}{n}\sum_{i=1}^{n}|y_i - \hat{y}_i| \quad (3)$$

where y_i and $\hat{y}_i$ are the measured and predicted LAI values, respectively, $\bar{y}$ is the mean of measured values, and n is the number of samples.

2.5.4 Model interpretation using SHAP

To maintain a consistent interpretation target across growth stages, SHAP analysis was conducted for the stage-specific TabPFN models using the fused feature set (Lundberg & Lee, 2017). For each stage, StandardScaler and TabPFN were refitted using all 70 observations and the corresponding fixed feature subset. KernelExplainer was used to approximate SHAP values. A representative subset of the standardised training data served as the background dataset, and 200 Monte Carlo samples were used for the approximation. SHAP values were computed for all 70 observations.

Global importance was quantified as the mean absolute SHAP value for each feature and expressed as a percentage of the sum across all retained features. SHAP dependence plots were generated for the highest-ranked predictors to describe nonlinear associations between feature values and model outputs. SHAP results were interpreted as post hoc statistical contributions within the fitted model, rather than as evidence of physiological causality.

2.6 Soil water–salinity correlation analysis

At each growth stage, the key features identified by SHAP and the soil SWC and $EC_{1:5}$ values were aggregated to treatment means (n = 7). Spearman rank correlations were used to assess monotonic associations, with a two-sided $p < 0.05$ considered statistically significant. No adjustment for multiple testing was applied; the correlations were therefore interpreted as exploratory evidence and were not used for causal inference (Spearman, 1904).

2.7 Spatial mapping of LAI

On the basis of cross-validation results across models and data sources, the TabPFN model using fused features showed the best overall predictive performance and was therefore selected for LAI mapping. For each growth stage, a final TabPFN model was refitted using all available observations and the corresponding fixed fused feature subset. The resulting stage-specific models were then applied to the corresponding multisource remote-sensing predictors to generate field-scale LAI maps for the four growth stages.

3. Results

3.1 Statistical characteristics of ground-measured LAI

Measured LAI followed a clear unimodal pattern across cotton growth stages. LAI peaked at flowering (4.03 ± 1.02), exceeding values at squaring (3.15 ± 0.58), boll development (2.85 ± 0.58), and boll opening (1.89 ± 0.50) (Table 1). Flowering showed the greatest absolute variability (SD = 1.02), whereas boll opening had the greatest relative variability (CV = 26.4%) because of its lower mean LAI. The maximum LAI observed at flowering (5.8) appeared as an upper outlier in the boxplot, indicating local heterogeneity in canopy development that may have been associated with favourable soil water–salinity conditions.

Table 1. Descriptive statistics of measured LAI.

Growth stage	Max	Min	Mean ± SD	Median	CV (%)
Squaring	4.5	2.1	3.15 ± 0.58	3.05	18.3
Flowering	5.8	2.4	4.03 ± 1.02	4.1	25.2
Boll development	4.2	1.8	2.85 ± 0.58	2.75	20.3
Boll opening	2.8	0.9	1.89 ± 0.50	1.8	26.4

Note: SD, standard deviation; CV, coefficient of variation.

3.2 Stable feature-selection results

As shown in Fig. 2a, the fused feature set retained 25, 26, 18, and 14 stable predictors at squaring, flowering, boll development, and boll opening, respectively. The hyperspectral dataset retained fewer features (8–14), whereas the RGB dataset retained an intermediate number (13–17).

Figs. 2b–e show the selection frequencies of fused features at the four growth stages. Mean, NDRE, VARI, HOM, and SEC were retained at multiple stages, indicating relatively consistent contributions to LAI estimation. WI_H had high selection frequencies at squaring, flowering, and boll opening but was not retained at boll development. The composition of the stable feature subsets varied across growth stages. Texture features were retained more frequently at squaring; both spectral and texture features contributed at flowering; RGB vegetation indices and senescence-related spectral indices became more prominent at boll development; and the number of retained features decreased markedly at boll opening. Overall, the fused feature subsets comprised hyperspectral vegetation indices, RGB colour indices, and texture metrics, with stage-specific differences in composition.

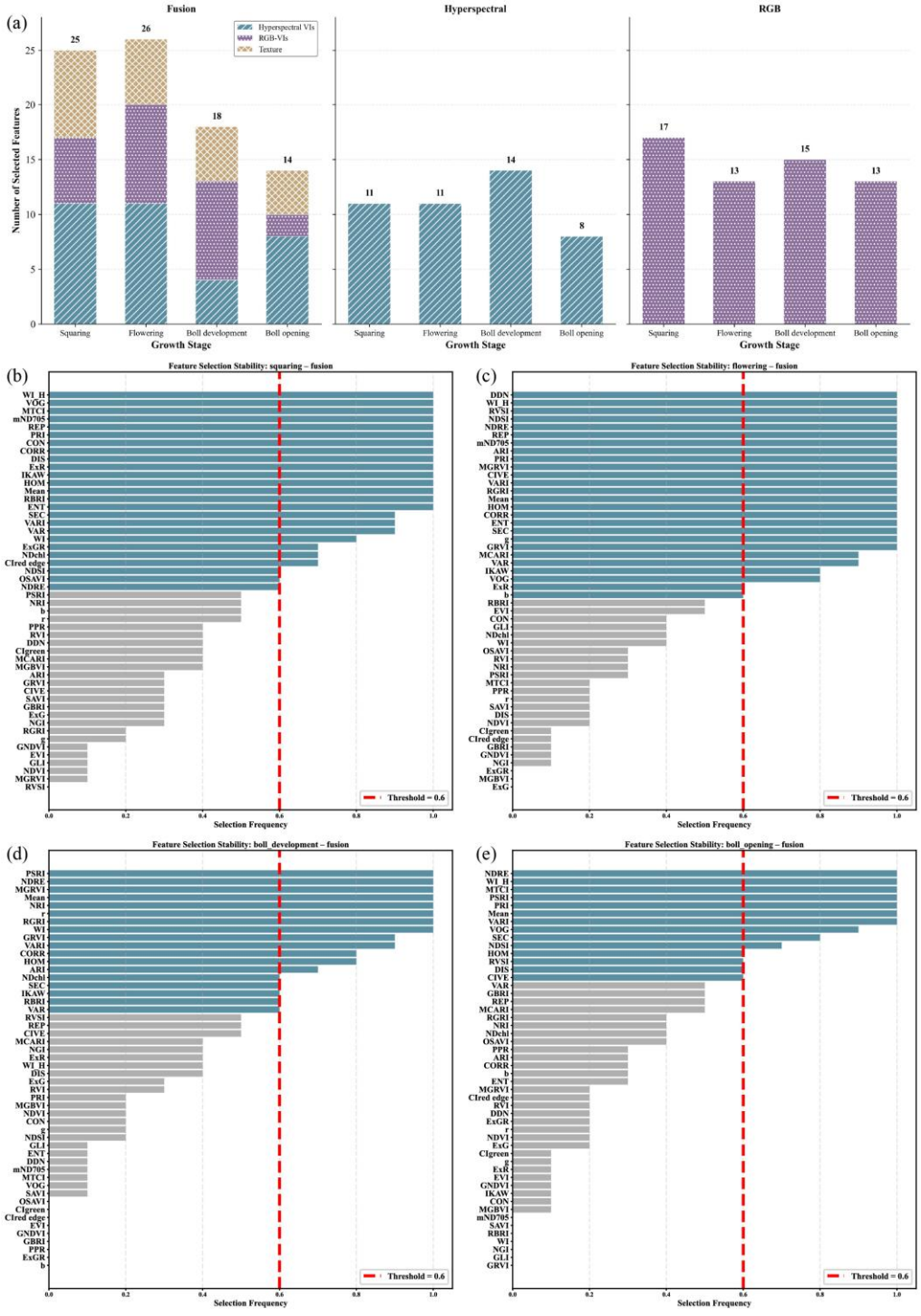


Fig. 2. RFECV-based feature-selection results. (a) Number of selected features from the hyperspectral, RGB, and fused datasets across four cotton growth stages. (b–e) Feature-selection stability for the fused dataset at squaring, flowering, boll development, and boll opening, respectively. Blue bars indicate features with a selection frequency ≥ 0.6, whereas grey bars indicate features below this threshold.

3.3 Comparative model performance

3.3.1 Overall performance

Under the fixed stable feature subsets, TabPFN achieved the best overall performance across the 12 growth-stage–feature-set combinations (Table 2). Across all 60 outer test folds (12 combinations × five folds), its mean R^2, RMSE, and MAE were 0.781 ± 0.190, 0.279 ± 0.178, and 0.143 ± 0.106, respectively. The corresponding mean R^2 values for XGBoost, random forest, and SVR were 0.616 ± 0.249, 0.612 ± 0.186, and 0.239 ± 1.032. TabPFN achieved the highest R^2 in 11 of the 12 combinations; the exception was the fused feature set at squaring, for which SVR (0.867 ± 0.087) outperformed TabPFN (0.826 ± 0.133).

Table 2. Overall model performance.

Model	Mean R^2 ± SD	Mean RMSE ± SD	Mean MAE ± SD
TabPFN	0.781 ± 0.190	0.279 ± 0.178	0.143 ± 0.106
XGBoost	0.616 ± 0.249	0.374 ± 0.204	0.249 ± 0.137
Random forest	0.612 ± 0.186	0.384 ± 0.163	0.307 ± 0.134
SVR	0.239 ± 1.032	0.483 ± 0.373	0.318 ± 0.212

Note: Means and standard deviations were calculated from 60 outer-test-fold scores for each model.

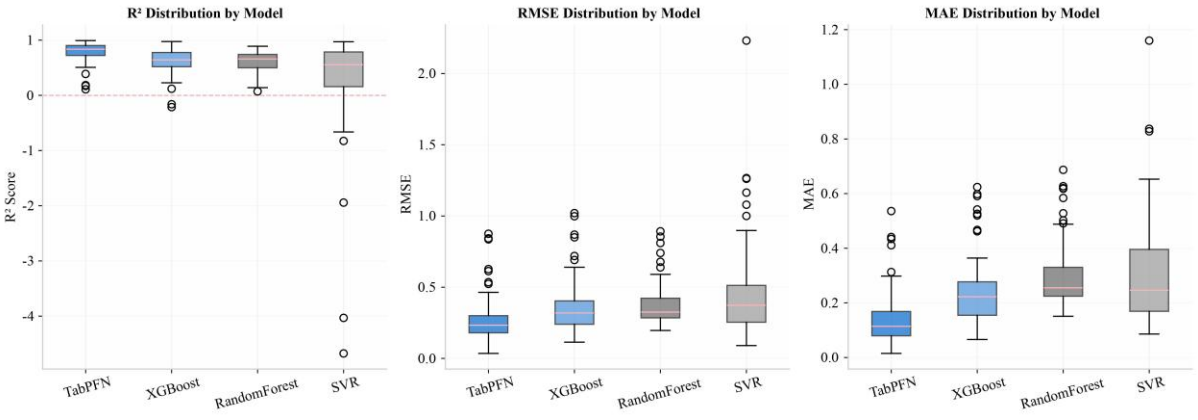


Fig. 3. Distributions of R^2, RMSE, and MAE by model.

The fold-level distributions shown in Fig. 3 were consistent with the summary statistics in Table 2. TabPFN had the highest median R^2 and the lowest median RMSE and MAE, together with relatively narrow interquartile ranges. XGBoost and random forest showed intermediate performance, whereas SVR had the widest distributions and several extreme values, including markedly negative R^2 values and unusually high RMSE and MAE. Overall, TabPFN provided the strongest and most consistent predictive performance across the evaluated growth stages and data sources.

3.3.2 Performance across feature sources and growth stages

Table 3 summarises model performance by feature source, and Fig. 4 further illustrates variation in R^2 across models, feature sources, and growth stages. Overall, the fused feature set achieved the highest mean R^2 (0.718 ± 0.379) and the lowest mean RMSE (0.298), outperforming the hyperspectral feature set (R^2 = 0.510 ± 0.632; RMSE = 0.397) and the RGB feature set (R^2 = 0.457 ± 0.657; RMSE = 0.445).

Table 3. Performance by feature source.

Feature source	Mean R^2	SD of R^2	Mean RMSE
Fused	0.718	0.379	0.298
Hyperspectral	0.510	0.632	0.397
RGB	0.457	0.657	0.445

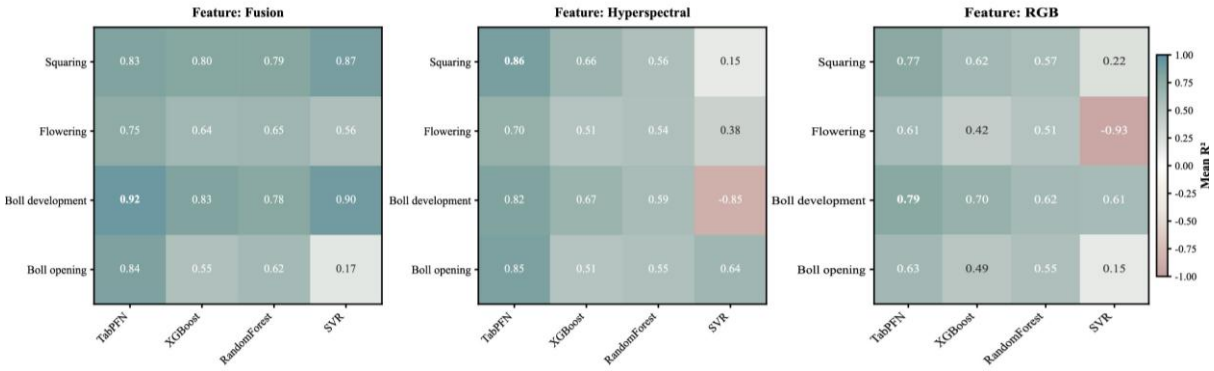


Fig. 4. R^2 heatmaps by feature source, model, and growth stage.

As shown in Fig. 4, TabPFN achieved the best or near-best performance in most combinations and maintained relatively high R^2 values across feature sources and growth stages. Thus, LAI estimation performance depended jointly on feature source, growth stage, and model type.

3.3.3 Predicted-versus-observed analysis

Fig. 5 shows the predicted-versus-observed relationships for TabPFN using fused features at the four growth stages. Predictions generally agreed well with measured LAI values. Performance was highest at boll development (R^2 = 0.920 ± 0.101; RMSE = 0.126). Squaring also showed high accuracy (R^2 = 0.826 ± 0.133; RMSE = 0.205), although higher LAI values were slightly underestimated. Flowering showed the greatest scatter (R^2 = 0.753 ± 0.361; RMSE = 0.407), indicating greater prediction uncertainty. Accuracy improved again at boll opening (R^2 = 0.842 ± 0.077; RMSE = 0.185).

Compared with the benchmark models shown in Supplementary Figs. S3–S5, TabPFN maintained close agreement across all growth stages and produced no obvious extreme predictions. XGBoost and random forest tended to underestimate high LAI values, whereas SVR produced large deviations at some stages. These scatterplots were consistent with the cross-validation rankings and further supported the predictive stability of TabPFN under different canopy conditions.

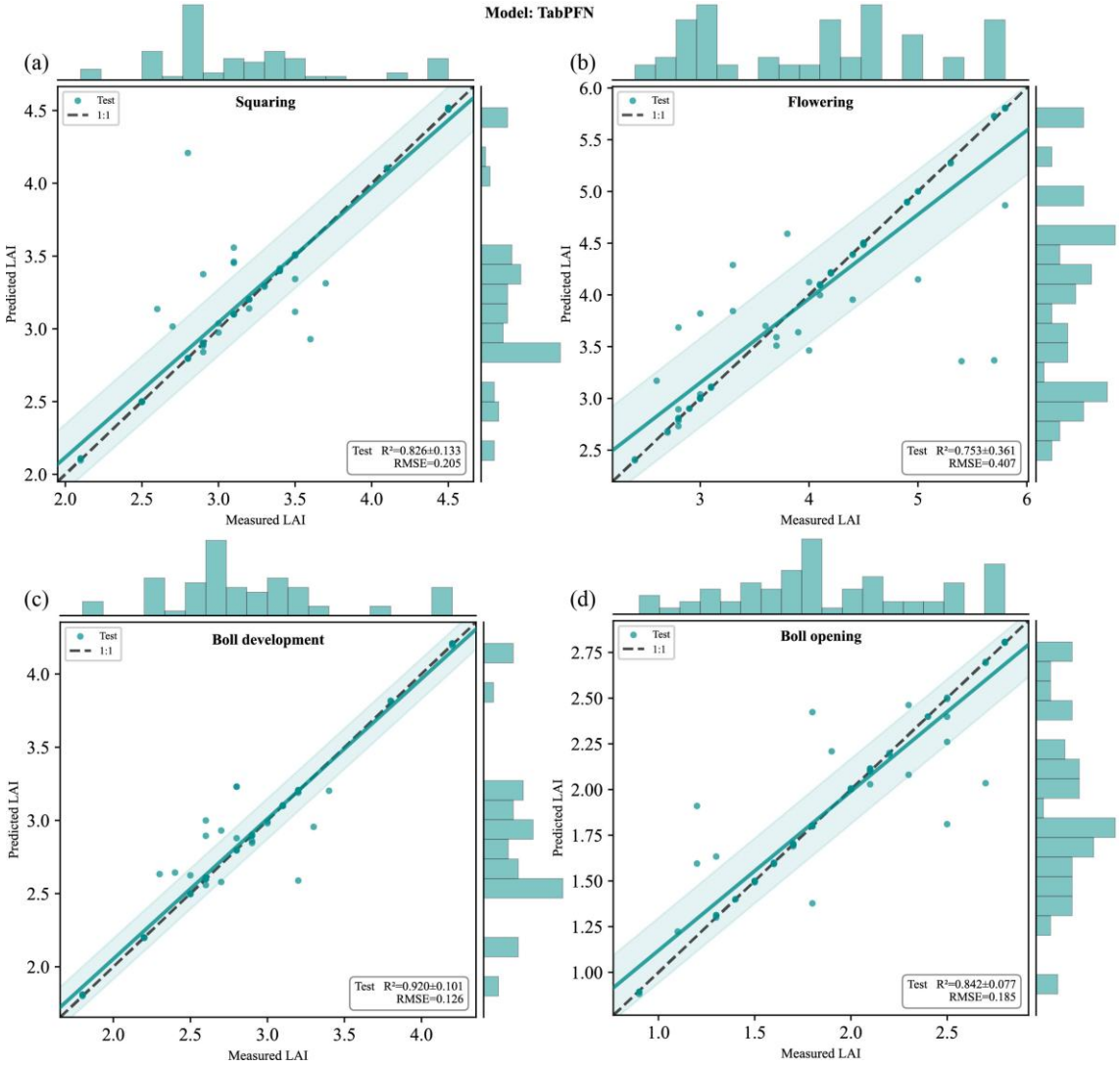


Fig. 5. Predicted-versus-observed 1:1 scatter plots for TabPFN using fused features. (a) Squaring; (b) flowering; (c) boll development; and (d) boll opening. Each panel pools test-set predictions from all five folds, with marginal histograms along the top and right axes. The dashed black line is the 1:1 reference. Insets report the mean ± SD of fold-specific R^2 values and the mean RMSE. Corresponding scatterplots for XGBoost, random forest, and SVR are provided in Supplementary Figs. S3–S5.

3.4 Effectiveness of multisource fusion

To quantify the contribution of multisource data fusion, the highest R^2 values obtained from the three feature sources were compared at each growth stage (Fig. 6). Fused features achieved the highest R^2 at squaring, flowering, and boll development, with values of 0.87, 0.75, and 0.92, respectively. These represented improvements of 1.2%, 7.1%, and 12.2% over the best-performing single-source feature set. At boll opening, hyperspectral features slightly outperformed fused features (0.85 vs 0.84), corresponding to a 1.2% decrease. The benefit of multisource fusion was therefore most evident at flowering and boll development, whereas its added value was limited when hyperspectral features alone already performed well.

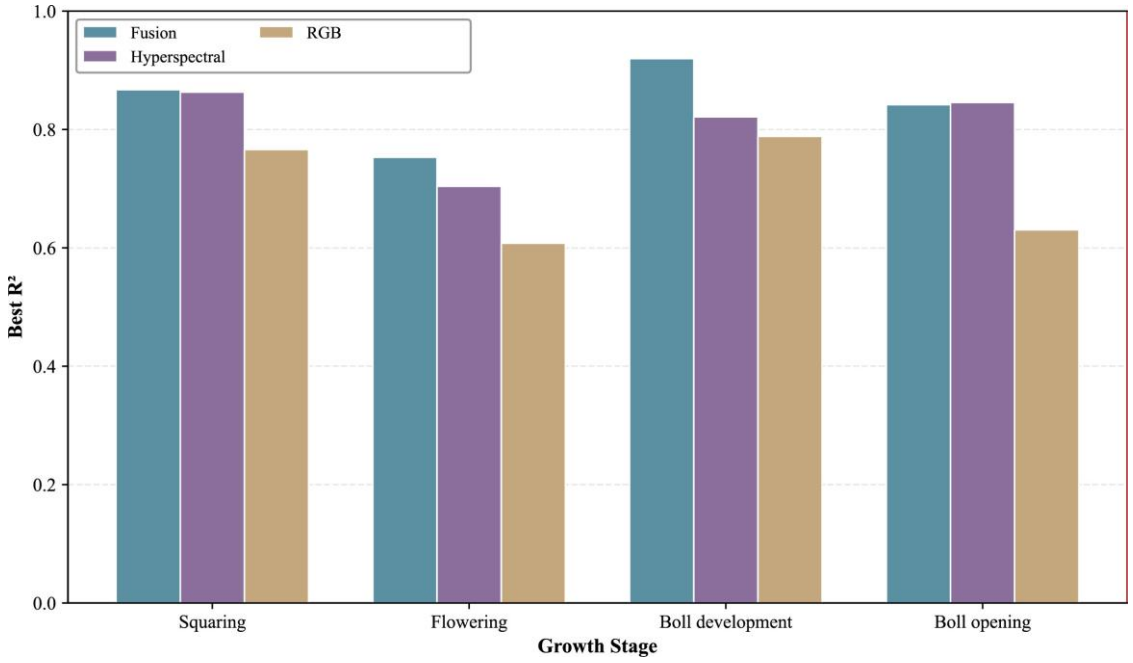


Fig. 6. Highest R^2 values obtained using fused, hyperspectral, and RGB feature sets at four cotton growth stages.

3.5 SHAP-based model interpretation

SHAP analysis of the TabPFN models using fused features showed that the dominant predictors differed among growth stages (Fig. 7). At squaring, CORR had the highest normalised relative importance (23.9%), followed by SEC (12.7%) and ENT (9.9%). At flowering, PRI ranked first (22.4%), followed by ARI (10.7%). At boll development, ARI was the most important predictor (23.7%), while CORR remained influential (14.5%). At boll opening, PRI made the largest contribution (35.5%).

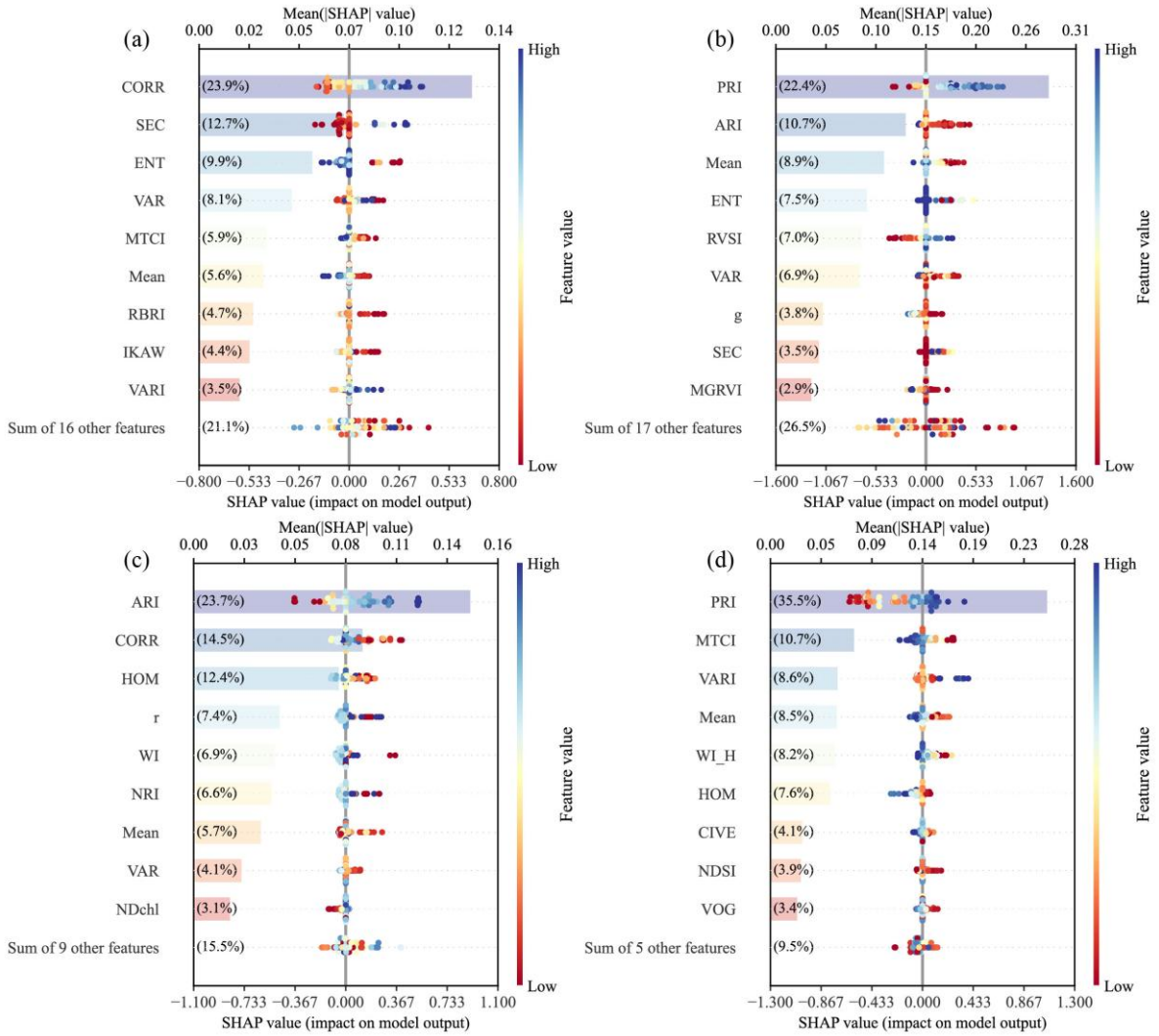


Fig. 7. SHAP beeswarm summary plots by growth stage: (a) squaring, (b) flowering, (c) boll development, and (d) boll opening. Colours indicate feature values (blue = high; red = low), and bar width represents mean |SHAP|.

Fig. 8 presents SHAP dependence plots for the top-ranked feature at each stage. The relationships were nonlinear. At squaring, CORR was generally associated with positive SHAP contributions. At flowering, PRI shifted from negative contributions at low values to positive contributions at high values. At boll development, positive contributions generally increased with ARI, whereas at boll opening, PRI produced clearly positive contributions mainly at the upper end of its range.

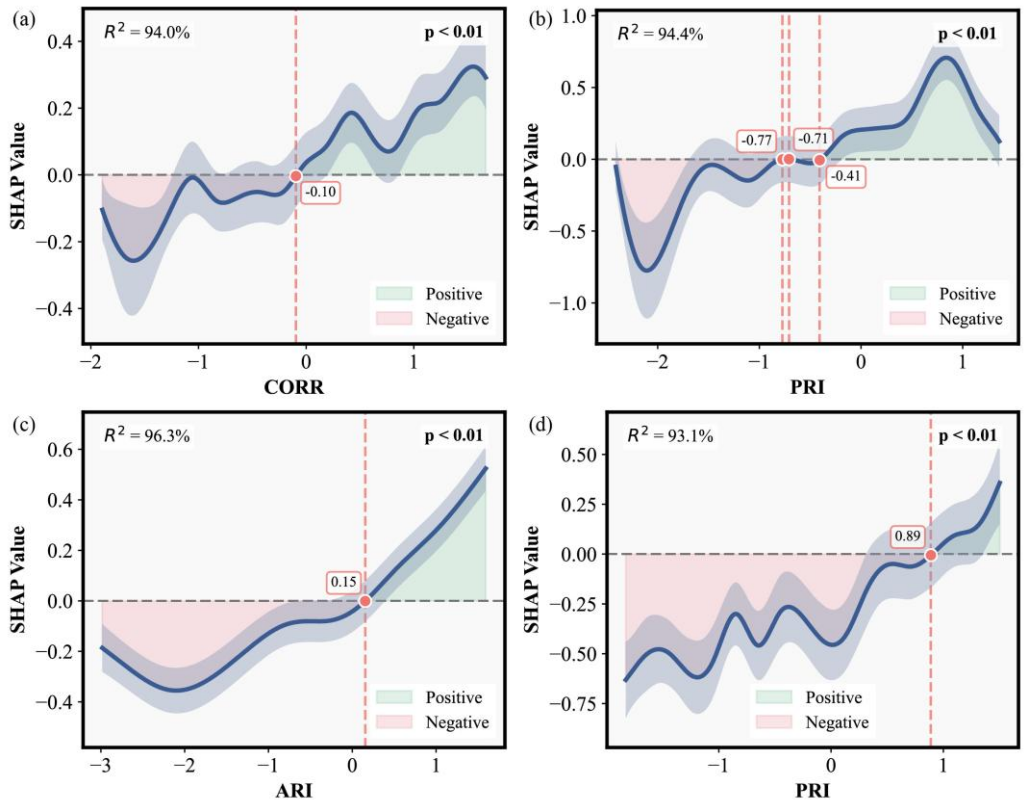


Fig. 8. SHAP dependence plots for the top-ranked feature at each stage: (a) CORR at squaring, (b) PRI at flowering, (c) ARI at boll development, and (d) PRI at boll opening. The blue curve shows the LOESS-smoothed trend, and the shaded band indicates the 95% confidence interval.

3.6 Relationships between soil water–salinity variables and LAI-related remote-sensing features

Treatment-level Spearman analysis revealed growth-stage-specific associations between key features and soil water–salinity variables. At squaring, VAR and Mean were positively correlated with SWC ($\rho = 0.857$ and 0.714, respectively). At flowering, RVSI was negatively correlated with SWC ($\rho = -0.857$). At boll development, ARI was strongly negatively correlated with EC ($\rho = -0.964$, $p < 0.01$), and NRI was negatively correlated with SWC ($\rho = -0.857$, $p < 0.05$). At boll opening, NDSI was positively correlated with SWC, whereas VOG was negatively correlated with EC. Additional associations are shown in Fig. 9.

Because each growth-stage analysis was based on only seven treatment means and no adjustment for multiple comparisons was applied, these results were interpreted as exploratory associations rather than evidence of direct causal relationships among soil water status, salinity, remote-sensing features, and LAI.

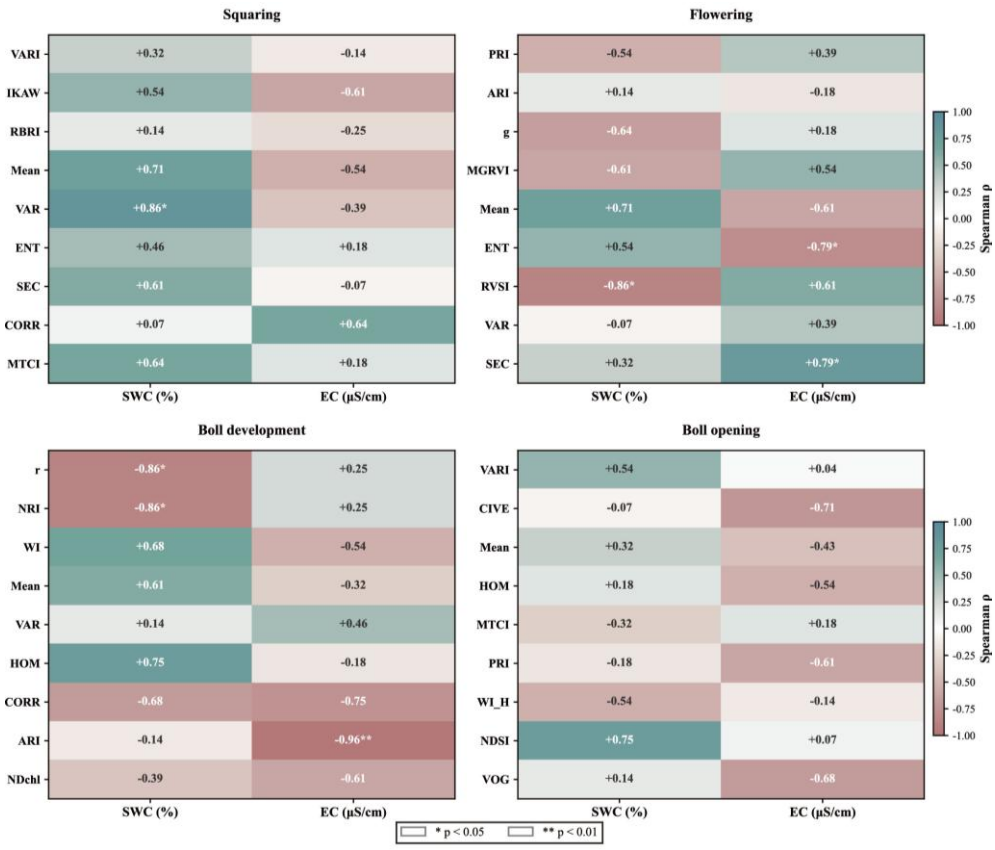


Fig. 9. Correlation heatmaps between SHAP-identified key features and soil water–salinity variables.

3.7 Spatial patterns of predicted LAI

The predicted LAI maps revealed clear spatial heterogeneity across growth stages and irrigation treatments (Fig. 10). Relatively high LAI values generally occurred in the CK, D1W3, and D1W2 plots, whereas lower values occurred in the D2W1, D2W2, and D1W1 plots. Spatial variation was also evident within individual plots, indicating heterogeneous canopy development under the different irrigation treatments. These maps were used to characterise field-scale LAI patterns and were not considered independent model-validation results.

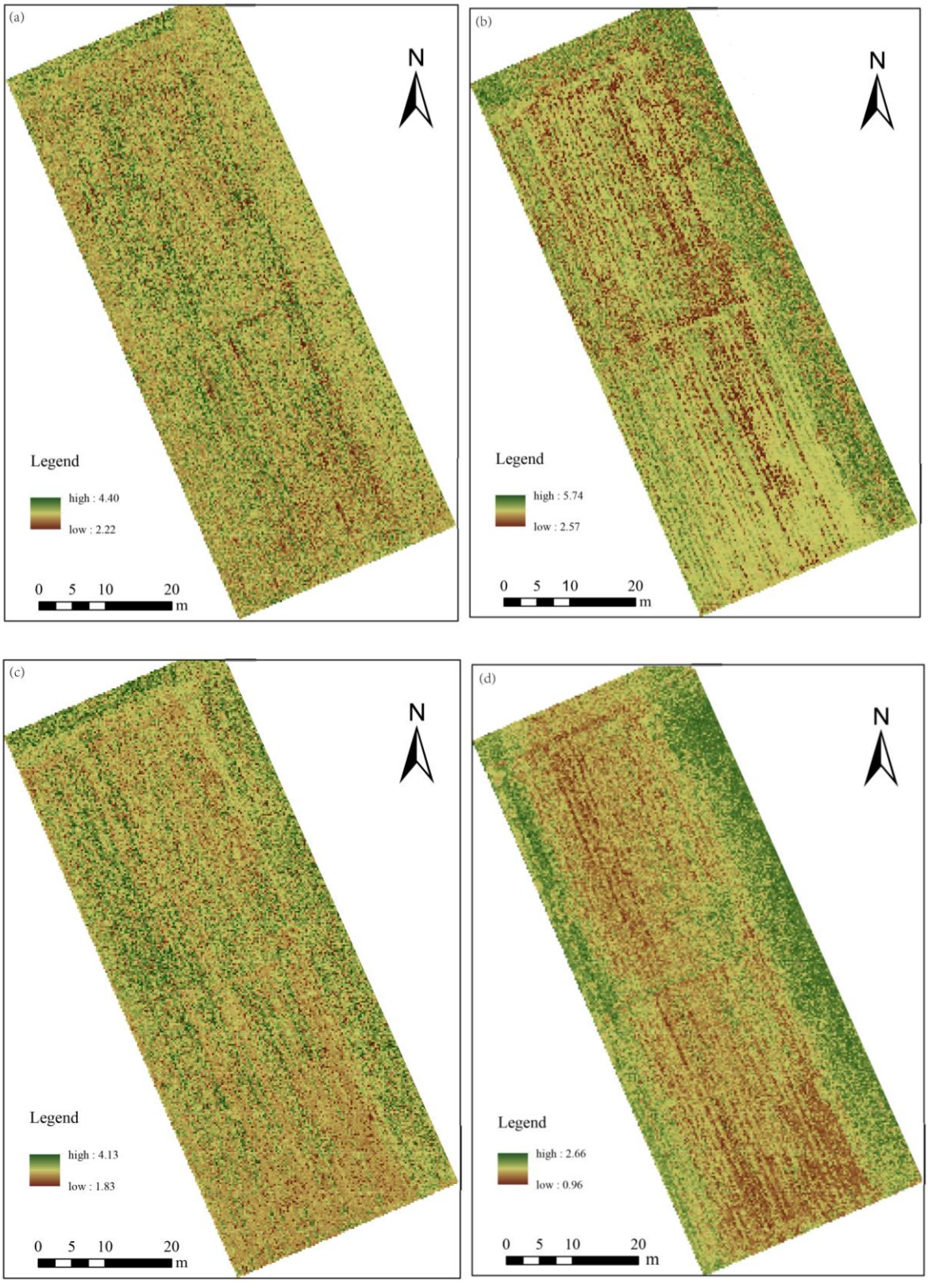


Fig. 10. Spatial distribution of LAI at each growth stage: (a) squaring, (b) flowering, (c) boll development, and (d) boll opening.

4. Discussion

4.1 Performance of TabPFN for small-sample cotton LAI estimation

The principal finding was that TabPFN achieved the strongest overall internal cross-validation performance under the fixed stable feature subsets. Across the 60 outer test folds, the mean R^2 was 0.781 ± 0.190, and the mean RMSE and MAE were 0.279 ± 0.178 and 0.143 ± 0.106, respectively. TabPFN achieved the highest R^2 in 11 of the 12 growth-stage–feature-set combinations. These results highlight the potential of TabPFN for cotton LAI estimation in a small-sample, multivariable setting, in which only 70 labelled observations were available at each growth stage and the candidate predictors were potentially correlated.

The overall advantage of TabPFN may be attributable to its pretrained representation and in-context learning mechanism. The model learns general statistical regularities from numerous synthetic tabular tasks and conditions its predictions for a new task on the available labelled observations (Hollmann et al., 2025). This mechanism may reduce dependence on extensive task-specific optimisation when training data are limited. In the present workflow, TabPFN was applied using a prespecified pretrained configuration, whereas XGBoost, random forest, and SVR required explicit hyperparameter selection within inner cross-validation. The markedly negative R^2 values obtained by SVR in several combinations indicated less consistent performance across growth stages and data sources.

Nevertheless, TabPFN was not superior in every combination. For the fused feature set at squaring, SVR achieved a mean R^2 of 0.867, compared with 0.826 for TabPFN. The findings therefore support an overall advantage of TabPFN across the evaluated combinations rather than universal superiority for every dataset. Moreover, because the stable feature subsets were identified from the complete stage-specific datasets before outer cross-validation, the reported performance may contain optimistic bias (Vabalas et al., 2019; Varma & Simon, 2006). The results should therefore be interpreted as internal model comparisons under the same experimental conditions, rather than as independent estimates of generalisation to other years, sites, or cultivation conditions.

4.2 Growth-stage dependence of multisource fusion

The benefit of multisource fusion was strongly growth-stage dependent (Fig. 6). Relative to the best-performing single-source feature set, fusion increased R^2 by 1.2%, 7.1%, and 12.2% at squaring, flowering, and boll development, respectively, but was 1.2% lower at boll opening. Thus, the value of fusion depended on the complementarity of information under a given canopy condition, rather than simply on the number of predictors.

At flowering and boll development, high canopy cover and the simultaneous presence of leaves, branches, and reproductive organs increased structural complexity, while pigment and photochemical status remained dynamic. Hyperspectral indices characterised red-edge, pigment-related, and photochemical information, whereas RGB colour and texture features added information on canopy continuity, shadows, and spatial arrangement. Similar benefits of integrating spectral and texture information have been reported for LAI estimation in maize, winter wheat, and rice (Sun et al., 2023; Zou et al., 2024; Li et al., 2024), while fusing multiple vegetation indices has also improved cotton LAI estimation (Fan et al., 2024).

At squaring, the relatively open canopy allowed either hyperspectral or RGB information alone to capture much of the LAI variation, limiting the additional benefit of fusion. At boll opening, senescence and pigment changes may have provided the dominant signals of LAI variation, consistent with the slight advantage of hyperspectral features. Phenotyping strategies should therefore select sensors and predictors according to developmental stage, rather than assuming that multisource fusion will invariably outperform a single data source.

4.3 Stage-specific feature contributions and soil water–salinity associations

SHAP analysis indicated a shift from texture-based structural information at squaring towards stronger photochemical contributions at flowering and boll opening, with joint pigment-related and structural contributions at boll development. The high importance of CORR, SEC, and ENT at squaring is consistent with the spatial heterogeneity created by plants, exposed soil, and shadows in a canopy that had not yet fully closed. As the canopy developed, PRI, ARI, and related indices became more influential, indicating greater use of photochemical and pigment-related variation by the fitted models.

At boll development, ARI was strongly negatively correlated with soil EC ($\rho = -0.964$), indicating a close statistical association between salinity variation and pigment-related spectral responses. UAV hyperspectral studies have similarly shown that salinity variation in cotton fields can be indirectly reflected in canopy spectral features (Wang et al., 2024). However, the present correlations were based on only seven treatment means and were not adjusted for multiple testing; they therefore do not establish that salinity directly caused pigment changes or LAI decline.

SHAP values are post hoc explanations of the fitted model (Lundberg & Lee, 2017). Feature importance and dependence relationships describe how variables influence model output, rather than representing physiological mechanisms themselves. Combining SHAP results with independent measurements of leaf pigments, photosynthesis, canopy temperature, and plant water status would strengthen the biological interpretation of model contributions.

4.4 Limitations and future research

This study has several limitations. First, the experiment involved a single cotton cultivar and one growing season; model transferability across years, cultivars, and ecological regions therefore remains to be evaluated. Second, SHAP analysis and soil water–salinity correlations describe statistical associations rather than direct causal relationships. Future studies should incorporate physiological measurements of leaf pigments, photosynthesis, and plant water status and combine data-driven methods with crop-growth models such as DSSAT and APSIM to evaluate the physiological relevance of key remote-sensing features. Thermal infrared imagery could also be incorporated into the TabPFN framework, and simultaneous estimation of LAI, chlorophyll content, biomass, and plant height could be explored to further increase the value of the approach for crop monitoring and precision irrigation.

5. Conclusions

This study developed a framework for estimating cotton LAI under shallow subsurface drip irrigation by integrating UAV-based hyperspectral and RGB remote sensing with TabPFN. Under fixed stable feature subsets, TabPFN achieved the strongest overall internal cross-validation performance across the 12 growth-stage–feature-set combinations. Across 60 outer test folds, the mean R^2, RMSE, and MAE were 0.781 ± 0.190, 0.279 ± 0.178, and 0.143 ± 0.106, respectively, and TabPFN achieved the highest R^2 in 11 combinations.

The benefit of multisource fusion was strongly phenology dependent: it was greatest at flowering and boll development but did not exceed the performance of hyperspectral features at boll opening. SHAP results indicated that prediction at squaring relied primarily on canopy texture and structure, prediction at flowering and boll opening relied more strongly on photochemical information, and prediction at boll development used both pigment-related and structural information. Field-scale LAI maps further characterised spatial differences among irrigation treatments.

Overall, combining TabPFN with UAV-based multisource remote sensing provides an interpretable framework for small-sample cotton phenotyping in arid regions. The present evidence primarily reflects internal predictive ability under the same experimental conditions; independent validation across years, sites, and spatial blocks is required before the framework can be generalised for precision-irrigation decision-making.

Declarations

Abbreviations

ARI, anthocyanin reflectance index; CIVE, colour index of vegetation extraction; CK, control; CON, contrast; CORR, correlation; CV, coefficient of variation; DIS, dissimilarity; DOY, day of year; EC, electrical conductivity; ENT, entropy; EVI, enhanced vegetation index; ExG, excess green index; FWHM, full width at half maximum; GCP, ground control point; GLCM, grey-level co-occurrence matrix; GRVI, green‐red vegetation index; HOM, homogeneity; LAI, leaf area index; MAE, mean absolute error; MTCI, MERIS terrestrial

chlorophyll index; NDRE, normalised difference red-edge index; NDVI, normalised difference vegetation index; NGRDI, normalised green–red difference index; PRI, photochemical reflectance index; REP, red-edge position; RF, random forest; RFECV, recursive feature elimination with cross-validation; RMSE, root mean square error; ROI, region of interest; SAVI, soil-adjusted vegetation index; SEC, angular second moment; SHAP, SHapley Additive exPlanations; SSDI, shallow subsurface drip irrigation; SVR, support vector regression; SWC, soil water content; TabPFN, Tabular Prior-data Fitted Network; UAV, unmanned aerial vehicle; VAR, variance; VARI, visible atmospherically resistant index; VOG, Vogelmann red-edge index; XGBoost, extreme gradient boosting.

Ethics approval and consent to participate

Not applicable.

Consent for publication

Not applicable.

Availability of data and materials

The datasets used and analysed during the current study are available from the corresponding author on reasonable request.

Competing interests

The authors declare no competing interests.

Funding

This work was supported by the National Natural Science Foundation of China (No. 52479044), the Key Technologies for Saline-Alkali Land Management in the Desert–Oasis Transition Zone of Southern Xinjiang (No. 2025AB047), and the Postgraduate Research Innovation Project of Tarim University (No. TDBSCX202522).

Authors' contributions

Fujun Meng: Data curation; Writing – original draft; Writing – review and editing. Yu Zhou: Writing – original draft; Writing – review and editing. Xingpeng Wang: Conceptualisation; Resources. Yujin Liu: Data curation. Aijun Sun: Resources. Yasengjiang Kahaer: Investigation. Shengru Yue: Visualisation; Writing – review and editing.

Acknowledgements

Not applicable.

References

Bendig, J., Yu, K., Aasen, H., Bolten, A., Bennertz, S., Broscheit, J., Gnyp, M. L., & Bareth, G. (2015). Combining UAV-based plant height from crop surface models, visible, and near infrared vegetation indices for biomass monitoring in barley. *International Journal of Applied Earth Observation and Geoinformation*, 39, 79–87. https://doi.org/10.1016/j.jag.2015.02.012

Breiman, L. (2001). Random forests. *Machine Learning*, 45(1), 5–32. https://doi.org/10.1023/A:1010933404324

Chen, T. & Guestrin, C. (2016). XGBoost: A scalable tree boosting system. In *Proceedings of the 22nd ACM SIGKDD International Conference on Knowledge Discovery and Data Mining* (pp. 785–794). ACM. https://doi.org/10.1145/2939672.2939785

Dash, J. & Curran, P. J. (2004). The MERIS terrestrial chlorophyll index. *International Journal of Remote Sensing*, 25(23), 5403–5413. https://doi.org/10.1080/0143116042000274015

Daughtry, C. S. T., Walthall, C. L., Kim, M. S., Brown de Colstoun, E., & McMurtrey III, J. E. (2000). Estimating corn leaf chlorophyll concentration from leaf and canopy reflectance. *Remote Sensing of Environment*, 74(2), 229–239. https://doi.org/10.1016/S0034-4257(00)00113-9

Duan, J., Li, N., Wang, J., Li, J., Hao, X., Luo, H., & Yang, G. (2021). Effect of embedded depth of drip irrigation belt on yield formation of cotton without plastic mulching. *Cotton Science*, 33(5), 404–411 (in Chinese). https://doi.org/10.11963/cs20210029

Fan, X., Gao, P., Zhang, M., Cang, H., Zhang, L., Zhang, Z., Wang, J., Lv, X., Zhang, Q., & Ma, L. (2024). The fusion of vegetation indices increases the accuracy of cotton leaf area prediction. *Frontiers in Plant Science*, 15, 1357193. https://doi.org/10.3389/fpls.2024.1357193

Fang, H., Baret, F., Plummer, S., & Schaepman-Strub, G. (2019). An overview of global leaf area index (LAI): Methods, products, validation, and applications. *Reviews of Geophysics*, 57(3), 739–799. https://doi.org/10.1029/2018RG000608

Fitzgerald, G. J., Rodriguez, D., Christensen, L. K., Belford, R., Sadras, V. O., & Clarke, T. R. (2006). Spectral and thermal sensing for nitrogen and water status in rainfed and irrigated wheat environments. *Precision Agriculture*, 7(4), 233–248. https://doi.org/10.1007/s11119-006-9011-z

Gale, F., Valdes, C., & Ash, M. (2022). Chinese cotton: textiles, imports, and Xinjiang. Economic Research Report No. 307. USDA Economic Research Service.

Gitelson, A. A., Kaufman, Y. J., & Merzlyak, M. N. (1996). Use of a green channel in remote sensing of global vegetation from EOS-MODIS. *Remote Sensing of Environment*, 58(3), 289–298. https://doi.org/10.1016/S0034-4257(96)00072-7

Gitelson, A. A., Merzlyak, M. N., & Chivkunova, O. B. (2001). Optical properties and nondestructive estimation of anthocyanin content in plant leaves. *Photochemistry and Photobiology*, 74(1), 38–45. https://doi.org/10.1562/0031-8655(2001)074<0038:OPANEO>2.0.CO;2

Gitelson, A. A., Kaufman, Y. J., Stark, R., & Rundquist, D. (2002). Novel algorithms for remote estimation of vegetation fraction. *Remote Sensing of Environment*, 80(1), 76–87. https://doi.org/10.1016/S0034-4257(01)00289-9

Gitelson, A. A., Viña, A., Ciganda, V., Rundquist, D. C., & Arkebauer, T. J. (2005). Remote estimation of canopy chlorophyll content in crops. *Geophysical Research Letters*, 32(8), L08403. https://doi.org/10.1029/2005GL022688

Grinsztajn, L., Flöge, K., Key, O., Birkel, F., Jund, P., Roof, B., Jäger, B., Safaric, D., Alessi, S., Hayler, A., Manium, M., Yu, R., Jablonski, F., Hoo, S. B., Garg, A., Robertson, J., Bühler, M., Moroshan, V., Purucker, L., Cornu, C., Wehrhahn, L. C., Bonetto, A., Schölkopf, B., Gambhir, S., Hollmann, N., & Hutter, F. (2025). TabPFN-2.5: Advancing the state of the art in tabular foundation models. *arXiv*, 2511.08667. https://doi.org/10.48550/arXiv.2511.08667

Guyon, I., Weston, J., Barnhill, S., & Vapnik, V. (2002). Gene selection for cancer classification using support vector machines. *Machine Learning*, 46(1–3), 389–422. https://doi.org/10.1023/A:1012487302797

Guyot, G., Baret, F., & Major, D. J. (1988). High spectral resolution: determination of spectral shifts between the red and the near infrared. *International Archives of Photogrammetry and Remote Sensing*, 11, 750–760.

Haralick, R. M., Shanmugam, K., & Dinstein, I. (1973). Textural features for image classification. *IEEE Transactions on Systems, Man, and Cybernetics*, SMC-3(6), 610–621. https://doi.org/10.1109/TSMC.1973.4309314

Hollmann, N., Müller, S., Purucker, L., Krishnakumar, A., Körfer, M., Hoo, S. B., Schirrmeister, R. T., & Hutter, F. (2025). Accurate predictions on small data with a tabular foundation model. *Nature*, 637(8045), 319–326. https://doi.org/10.1038/s41586-024-08328-6

Huete, A. R. (1988). A soil-adjusted vegetation index (SAVI). *Remote Sensing of Environment*, 25(3), 295–309. https://doi.org/10.1016/0034-4257(88)90106-X

Huete, A., Didan, K., Miura, T., Rodriguez, E. P., Gao, X., & Ferreira, L. G. (2002). Overview of the radiometric and biophysical performance of the MODIS vegetation indices. *Remote Sensing of Environment*, 83(1–2), 195–213. https://doi.org/10.1016/S0034-4257(02)00096-2

Kang, X., Huang, C., Chen, J. M., Lv, X., Wang, J., Zhong, T., Wang, H., Fan, X., Ma, Y., Yi, X., Zhang, Z., Zhang, L., & Tong, Q. (2023). The 10-m cotton maps in Xinjiang, China during 2018–2021. *Scientific Data*, 10(1), 688. https://doi.org/10.1038/s41597-023-02584-3

Kawashima, S. & Nakatani, M. (1998). An algorithm for estimating chlorophyll content in leaves using a video camera. *Annals of Botany*, 81(1), 49–54. https://doi.org/10.1006/anbo.1997.0544

le Maire, G., François, C., & Dufrêne, E. (2004). Towards universal broad leaf chlorophyll indices using PROSPECT simulated database and hyperspectral reflectance measurements. *Remote Sensing of Environment*, 89(1), 1–28. https://doi.org/10.1016/j.rse.2003.09.004

Li, C., Teng, X., Tan, Y., Zhang, Y., Zhang, H., Xiao, D., & Luo, S. (2024). Spatio-temporal mapping of leaf area index in rice: Spectral indices and multi-scale texture comparison derived from different sensors. *Frontiers in Plant Science*, 15, 1445490. https://doi.org/10.3389/fpls.2024.1445490

Li, F., Mistele, B., Hu, Y., Chen, X., & Schmidhalter, U. (2013). Comparing hyperspectral index optimization algorithms to estimate aerial N uptake using multi-temporal winter wheat datasets from contrasting climatic and geographic zones in China and Germany. *Agricultural and Forest Meteorology*, 180, 44–57. https://doi.org/10.1016/j.agrformet.2013.05.003

Li, S., Yuan, F., Ata-Ul-Karim, S. T., Zheng, H., Cheng, T., Liu, X., Tian, Y., Zhu, Y., Cao, W., & Cao, Q. (2019). Combining color indices and textures of UAV-based digital imagery for rice LAI estimation. *Remote Sensing*, 11(15), 1763. https://doi.org/10.3390/rs11151763

Liu, S., Jin, X., Nie, C., Wang, S., Yu, X., Cheng, M., Shao, M., Wang, Z., Tuohuti, N., Bai, Y., & Liu, Y. (2021). Estimating leaf area index using unmanned aerial vehicle data: Shallow versus deep machine learning algorithms. *Plant Physiology*, 187(3), 1551–1576. https://doi.org/10.1093/plphys/kiab322

Louhaichi, M., Borman, M. M., & Johnson, D. E. (2001). Spatially located platform and aerial photography for documentation of grazing impacts on wheat. *Geocarto International*, 16(1), 65–70. https://doi.org/10.1080/10106040108542184

Lundberg, S. M. & Lee, S.-I. (2017). A unified approach to interpreting model predictions. *Advances in Neural Information Processing Systems*, 30, 4765–4774.

Ma, Y., Zhang, Q., Yi, X., Ma, L., Zhang, L., Huang, C., Zhang, Z., & Lv, X. (2022). Estimation of cotton leaf area index (LAI) based on spectral transformation and vegetation index. *Remote Sensing*, 14(1), 136. https://doi.org/10.3390/rs14010136

Merton, R. N. (1998). Monitoring community hysteresis using spectral shift analysis and the red-edge vegetation stress index. In *Proceedings of the Seventh Annual JPL Airborne Earth Science Workshop*. NASA Jet Propulsion Laboratory.

Merzlyak, M. N., Gitelson, A. A., Chivkunova, O. B., & Rakitin, V. Y. (1999). Non-destructive optical detection of pigment changes during leaf senescence and fruit ripening. *Physiologia Plantarum*, 106(1), 135–141. https://doi.org/10.1034/j.1399-3054.1999.106119.x

Metternicht, G. (2003). Vegetation indices derived from high-resolution airborne videography for precision crop management. *International Journal of Remote Sensing*, 24(14), 2855–2877. https://doi.org/10.1080/01431160210163074

Meyer, G. E. & Neto, J. C. (2008). Verification of color vegetation indices for automated crop imaging applications. *Computers and Electronics in Agriculture*, 63(2), 282–293. https://doi.org/10.1016/j.compag.2008.03.009

Mou, H., Liu, H., Zhang, X., Wang, Y., & Chen, J. (2011). Water and salt dynamics under drip irrigation in arid regions. *Agricultural Research in the Arid Areas*, 29(4), 78–83 (in Chinese).

Nogueira, S., Sechidis, K., & Brown, G. (2018). On the stability of feature selection algorithms. *Journal of Machine Learning Research*, 18(174), 1–54.

OECD/FAO (2025). OECD-FAO agricultural outlook 2025–2034: Cotton. OECD Publishing.

Pearson, R. L. & Miller, L. D. (1972). Remote mapping of standing crop biomass for estimation of the productivity of the shortgrass prairie. In *Proceedings of the 8th International Symposium on Remote Sensing of Environment* (pp. 1357–1381). Environmental Research Institute of Michigan.

Pedregosa, F., Varoquaux, G., Gramfort, A., Michel, V., Thirion, B., Grisel, O., Blondel, M., Prettenhofer, P., Weiss, R., Dubourg, V., Vanderplas, J., Passos, A., Cournapeau, D., Brucher, M., Perrot, M., & Duchesnay, É. (2011). Scikit-learn: machine learning in Python. *Journal of Machine Learning Research*, 12(85), 2825–2830.

Peñuelas, J., Piñol, J., Ogaya, R., & Filella, I. (1997). Estimation of plant water concentration by the reflectance water index WI (R900/R970). *International Journal of Remote Sensing*, 18(13), 2869–2875. https://doi.org/10.1080/014311697217396

Roy, P. K., Surekha, P., & Rajagopal, C. (2011). Surface oxidation of low-density polyethylene films to improve their susceptibility toward environmental degradation. *Journal of Applied Polymer Science*, 122(4), 2765–2773. https://doi.org/10.1002/app.34097

Sims, D. A. & Gamon, J. A. (2002). Relationships between leaf pigment content and spectral reflectance across a wide range of species, leaf structures and developmental stages. *Remote Sensing of Environment*, 81(2–3), 337–354. https://doi.org/10.1016/S0034-4257(02)00010-X

Smola, A. J. & Schölkopf, B. (2004). A tutorial on support vector regression. *Statistics and Computing*, 14(3), 199–222. https://doi.org/10.1023/B:STCO.0000035301.49549.88

Spearman, C. (1904). The proof and measurement of association between two things. *American Journal of Psychology*, 15(1), 72–101. https://doi.org/10.2307/1412159

Sun, X., Yang, Z., Su, P., Wei, K., Wang, Z., Yang, C., Wang, C., Qin, M., Xiao, L., Yang, W., Zhang, M., Song, X., & Feng, M. (2023). Non-destructive monitoring of maize LAI by fusing UAV spectral and textural features. *Frontiers in Plant Science*, 14, 1158837. https://doi.org/10.3389/fpls.2023.1158837

USDA Foreign Agricultural Service (2024). Cotton: world markets and trade. United States Department of Agriculture.

Vabalas, A., Gowen, E., Poliakoff, E., & Casson, A. J. (2019). Machine learning algorithm validation with a limited sample size. *PLoS ONE*, 14(11), e0224365. https://doi.org/10.1371/journal.pone.0224365

Varma, S. & Simon, R. (2006). Bias in error estimation when using cross-validation for model selection. *BMC Bioinformatics*, 7, 91. https://doi.org/10.1186/1471-2105-7-91

Vogelmann, J. E., Rock, B. N., & Moss, D. M. (1993). Red edge spectral measurements from sugar maple leaves. *International Journal of Remote Sensing*, 14(8), 1563–1575. https://doi.org/10.1080/01431169308953986

Wan, Y., Li, W., Wang, J., Wu, B., & Su, F. (2024). Effects of different drip irrigation rates on root distribution characteristics and yield of cotton under mulch-free cultivation in southern Xinjiang. *Water*, 16(8), 1148. https://doi.org/10.3390/w16081148

Wang, Z., Ding, J., Tan, J., Liu, J., Zhang, T., Cai, W., & Meng, S. (2024). UAV hyperspectral analysis of secondary salinization in arid oasis cotton fields: Effects of FOD feature selection and SOA-RF. *Frontiers in Plant Science*, 15, 1358965. https://doi.org/10.3389/fpls.2024.1358965

Woebbecke, D. M., Meyer, G. E., Von Bargen, K., & Mortensen, D. A. (1995). Color indices for weed identification under various soil, residue, and lighting conditions. *Transactions of the ASAE*, 38(1), 259–269. https://doi.org/10.13031/2013.27838

Yang, G., Liu, J., Zhao, C., Li, Z., Huang, Y., Yu, H., Xu, B., Yang, X., Zhu, D., Zhang, X., Zhang, R., Feng, H., Zhao, X., Li, Z., Li, H., & Yang, H. (2017). Unmanned aerial vehicle remote sensing for field-based crop phenotyping: current status and perspectives. *Frontiers in Plant Science*, 8, 1111. https://doi.org/10.3389/fpls.2017.01111

Yang, X., Chen, J., Lu, X., Liu, H., Liu, Y., Bai, X., Qian, L., & Zhang, Z. (2025). Advances in UAV remote sensing for monitoring crop water and nutrient status: modeling methods, influencing factors, and challenges. *Plants*, 14(16), 2544. https://doi.org/10.3390/plants14162544

Zhang, P. S., Sun, Y. M., Guo, P. T., Yuan, Z. Z., Yang, H. Z., Bei, M. R., & Luo, W. (2015). Study on predicting nitrogen content of rubber tree leaf by digital image analysis. *Chinese Journal of Tropical Crops*, 36(12), 2120–2124 (in Chinese). https://doi.org/10.3969/j.issn.1000-2561.2015.12.002

Zou, M., Liu, Y., Fu, M., Li, C., Zhou, Z., Meng, H., Xing, E., & Ren, Y. (2024). Combining spectral and texture feature of UAV image with plant height to improve LAI estimation of winter wheat at jointing stage. *Frontiers in Plant Science*, 14, 1272049. https://doi.org/10.3389/fpls.2023.1272049

Supplementary Files

This is a list of supplementary files associated with this preprint. Click to download.

- A1A3.docx
- SupplementaryFigsS1S9.docx